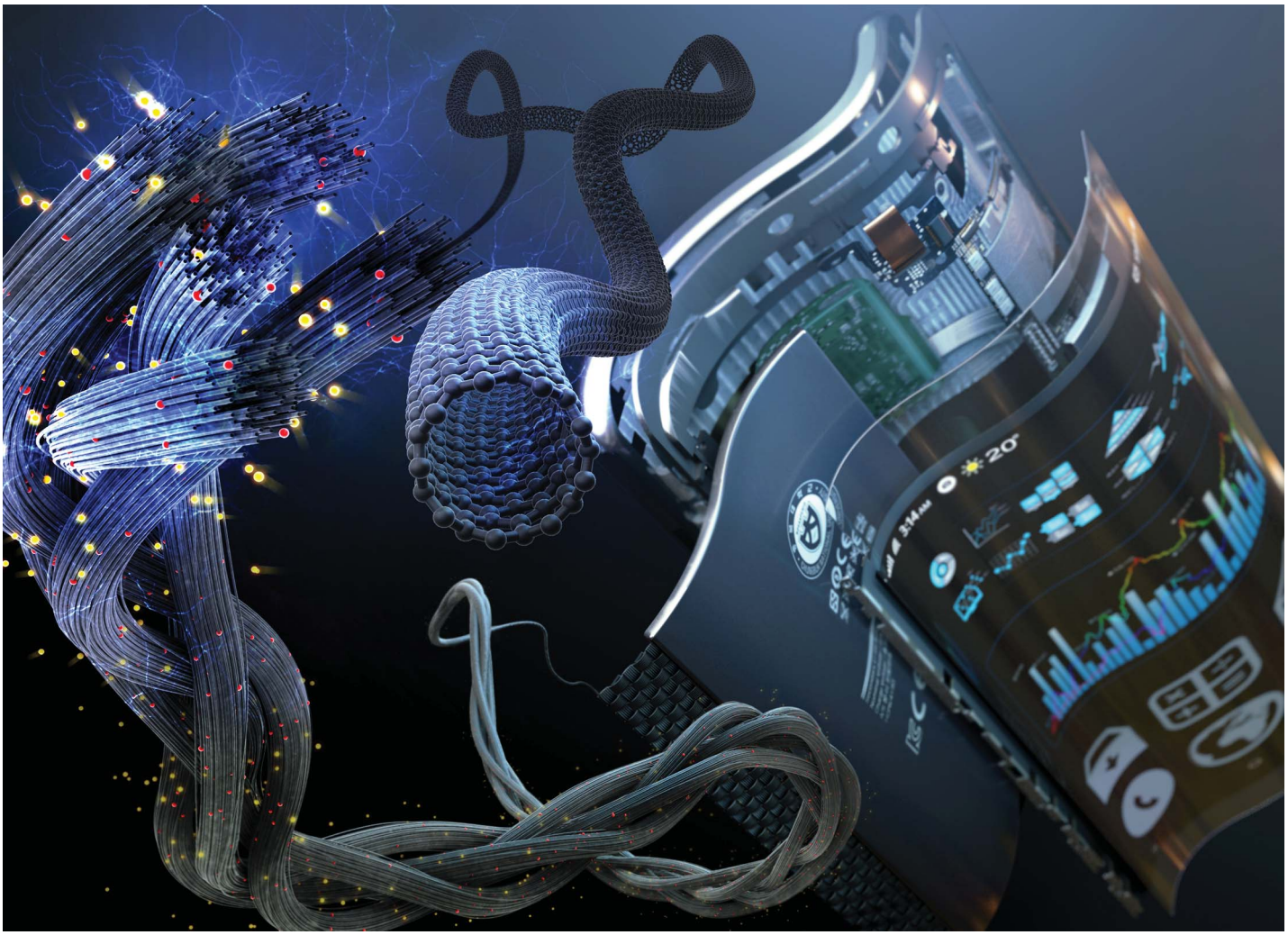

Flexible and stretchable rechargeable battery research from Prof. Jae-Kwang Kim's group of Cheongju University and Prof. Jung Sang Cho's group of Chungbuk National University, Republic of Korea.

Highly integrated and interconnected CNT hybrid nanofibers decorated with α-iron oxide as freestanding anodes for flexible lithium polymer batteries

Describing highly integrated and interconnected carbon nanotubes (CNTs) in the α-Fe_2O_3/CNT composite nanofiber conducted as an electron transfer pathway during repeated cycling in the flexible rechargeable lithium ion batteries. Numerous nanovoids between the CNTs facilitated the penetration of electrolyte which promoted Li^+ ion diffusion into the structure for flexible batteries.

As featured in:

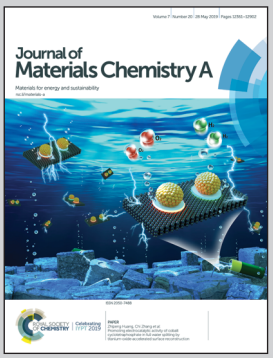

See Jae-Kwang Kim, Jung Sang Cho *et al.*, *J. Mater. Chem. A*, 2019, **7**, 12480.

ROYAL SOCIETY OF CHEMISTRY | Celebrating IYPT 2019

rsc.li/materials-a

Registered charity number: 207890

Journal of Materials Chemistry A

PAPER

View Article Online
View Journal | View Issue

Cite this: J. Mater. Chem. A, 2019, 7, 12480

Highly integrated and interconnected CNT hybrid nanofibers decorated with α-iron oxide as freestanding anodes for flexible lithium polymer batteries†

Se Hwan Oh,[a] O Hyeon Kwon,[b] Yun Chan Kang,[c] Jae-Kwang Kim*[b] and Jung Sang Cho*[a]

Received 4th February 2019
Accepted 27th March 2019

DOI: 10.1039/c9ta01374a

rsc.li/materials-a

Highly integrated and interconnected carbon nanotube (CNT) hybrid nanofibers decorated with α-Fe_2O_3 (denoted hereafter as HI-CNT/Fe_2O_3 nanofibers) were first introduced for potential use as freestanding anodes in flexible lithium polymer batteries. CNTs were modified to have a carboxyl group attached. Polyacrylonitrile (PAN) was also hydrolyzed, forming sulfonated polyacrylamide. Dipole–dipole interactions and hydrogen bonding between CNTs and PAN can form Fe(acac)$_3$–PAN–CNT complexes, thus allowing for the formation of highly integrated CNTs in a stable jet without being aggregated during electrospinning. The discharge capacity of a freestanding HI-CNT/Fe_2O_3 nanofiber anode after 100 cycles at 100 mA g^{-1} was 651 mA h g^{-1}. The specific capacity of a flexible full-cell combined with a $LiFePO_4$ cathode was maintained at 148.5 mA h g^{-1} (cathode-based) even after bending for 10 cycles as compared with 148.9 mA h g^{-1} before bending.

Introduction

With the rapid growth of the market for flexible and wearable electronic devices, improved properties of batteries have attracted much attention to supply high power for devices.[1–4] Lithium polymer batteries are the most suitable power sources for flexible and wearable electronic devices because of their higher energy density, higher output voltage, longer cycle life, and environmentally benign operation compared to other batteries such as alkaline batteries and supercapacitors.[5–9] However, lithium polymer batteries that are currently in use require enhancement of many electrochemical properties such as energy density, rate characteristics, and stability. Moreover, graphite-based conventional lithium ion batteries are unsuitable for high-energy density flexible polymer batteries because they are limited by their theoretical capacity of 372 mA h g^{-1}.[10–14]

Transition metal oxides (TMOs) could serve as alternatives for flexible lithium polymer batteries. They have been widely studied for decades.[15–19] Specifically, iron oxide materials that can store Li^+ ions *via* a conversion reaction have recently attracted increased attention as promising anode materials because of their high theoretical capacity (1007 mA h g^{-1}), nontoxicity, low cost, and safety.[20–23] These properties made them significantly important in applications such as flexible lithium polymer batteries. However, the large volume expansion during electrochemical reactions and the low electrical conductivity of α-Fe_2O_3 have led to a rapid capacity drop and large cell resistance as well as rigid inherent properties of α-Fe_2O_3, all of which hindered their practical application in flexible lithium polymer batteries. Therefore, a novel strategy is needed for α-Fe_2O_3 anode materials to be applied in flexible lithium polymer batteries with high energy density.[24–26]

Based on these viewpoints, highly integrated and interconnected CNT hybrid nanofibers decorated with α-Fe_2O_3 could be a tactic to solve these problems. CNTs in the composite functioned as an electron transfer pathway during repeated cycling. Numerous nanovoids between CNTs also facilitated the penetration of electrolyte which promoted Li^+ ion diffusion into the structure. Moreover, the CNT framework successfully reduced stress induced by volume variation of α-Fe_2O_3 particles by surrounding the particles and flexible system during cycling. Therefore, studies for synthesizing CNT composites with Fe_2O_3 prepared by diverse processes have been introduced. Gao *et al.*[27] prepared an Fe_2O_3/CNT composite, in which CNTs are *in situ* attached to Fe_2O_3 submicron spheres, by a hydrothermal process. Further, Yu *et al.*[28] filled Fe_2O_3 nanoparticles into the

[a]Department of Engineering Chemistry, Chungbuk National University, Chungbuk 361-763, Republic of Korea. E-mail: jscho@cbnu.ac.kr; Fax: +82-43-262-2380

[b]Department of Solar & Energy Engineering, Cheongju University, Cheongju, Chungbuk, 28503, Republic of Korea. E-mail: jaekwang@cju.ac.kr; Fax: +82-43-229-7322

[c]Department of Materials Science and Engineering, Korea University, Anam-Dong, Seongbuk-Gu, Seoul 136-713, Republic of Korea

† Electronic supplementary information (ESI) available. See DOI: 10.1039/c9ta01374a

hollow core of high aspect ratio CNTs *via* a chemical vapor deposition process. Bak *et al.*[29] deposited Fe_2O_3 nanoparticles on functionalized CNTs through a two-step process. Zhao *et al.*[30] produced Fe_2O_3-decorated CNTs with a "nanohorn" morphology by a hydrothermal method. Yan *et al.*[31] produced a hybrid nanostructure by coating Fe_2O_3 nanoparticles with multi-walled CNTs. However, to date, highly integrated and interconnected CNT hybrid nanofibers decorated with Fe_2O_3 nanoparticles have been scarcely studied. This is due to the agglomeration of CNTs in solutions caused by van der Waals forces, which impeded the synthesis of highly integrated CNT composites.

In this study, highly integrated and interconnected CNT hybrid nanofibers decorated with α-Fe_2O_3 were successfully prepared for flexible lithium polymer batteries. For this, CNTs were modified by having carboxyl groups attached using a HNO_3/H_2SO_4 solution. PAN was also hydrolyzed, forming sulfonated polyacrylamide. Therefore, dipole–dipole interactions and hydrogen bonding between CNTs and PAN can form $Fe(acac)_3$–PAN–CNT complexes which allows for the formation of a stable jet containing highly integrated CNTs without being aggregated during the electrospinning process. Highly integrated CNT hybrid nanofibers decorated with α-Fe_2O_3 showed superior cycle performance and rate performance as freestanding anodes for flexible Li^+ ion batteries due to the synergetic effects of their unique one-dimensional nanostructure and the highly integrated and interconnected CNTs. The formation mechanism of such unique hybrid nanofibers and their electrochemical properties as freestanding anodes for flexible lithium polymer batteries were investigated in detail.

Experimental

Sample preparation

Highly integrated and interconnected CNT hybrid nanofibers decorated with α-Fe_2O_3 were prepared by the electrospinning process with a subsequent simple heat-treatment. In particular, a colloidal solution for electrospinning was prepared by dissolving 3.0 g of iron(III) acetylacetonate [$Fe(acac)_3$, Junsei, 98.0%] and 1.5 g of sulfonated polyacrylonitrile [PAN, M_w: 150 000, Sigma-Aldrich] in a mixed solution containing 20 mL of dimethylformamide [DMF, Samchun, 99.8%] and 1.0 g of acid-treated CNTs. For this purpose, CNTs (MWCNTs, Cheap Tubes Inc., Cambridgeport, USA; OD: 20–30 nm, length: 10–30 μm, purity: >95.0 wt%) were modified using a HNO_3/H_2SO_4 (1 : 3 vol%) acid solution at 80 °C and washed with a solution of distilled water and ethyl alcohol. Subsequently, these acid-treated CNTs were freeze-dried. In order to prepare the spinning solution, PAN was also sulfonated beforehand with a H_2SO_4 acid solution at 80 °C. The prepared colloidal solution was loaded into a plastic syringe equipped with a 21-gauge stainless steel nozzle. The loaded solution was ejected at a flow rate of 2 mL h^{-1}. The rotation speed of the drum collector was set at 150 rpm. The distance between the tip and the collector was fixed at 15 cm. The voltage applied between the collector and the syringe tip was maintained at 25 kV. Precursor Fe(acac)/PAN/CNT composite nanofibers obtained after electrospinning were stabilized at 100 °C for 3 h in air. Finally, highly integrated and interconnected CNT hybrid nanofibers decorated with α-Fe_2O_3 were obtained after heat-treatment at 350 °C for 3 h in air. For simplicity, highly integrated CNT hybrid nanofibers decorated with α-Fe_2O_3 are referred to as "HI-CNT/Fe_2O_3 nanofibers" hereafter.

Gel-polymer electrolyte (GPE) preparation

A polyimide (PI)-based gel-polymer electrolyte (GPE) was prepared by electrospinning followed by subsequent imidization.[32] In order to obtain a poly (amic acid) (PAA) solution, 1,2,4,5-benzenetetracarboxylic dianhydride (PMDA) and 4,40-oxydianiline (ODA) were mixed together. A PAA matrix was then prepared by electrospinning. The as-prepared PAA matrix was converted into a PI matrix through a five-step heat treatment-induced imidization (at 70 °C for 30 min, 120 °C for 30 min, 200 °C for 60 min, 300 °C for 30 min, and 400 °C for 1 h) under nitrogen atmosphere. The gel-polymer electrolyte was prepared by soaking the electrospun PI matrix for 3 min in a solution of 1 M $LiPF_6$ in ethylene carbonate (EC)/dimethyl carbonate (DMC) (1 : 1 by vol.) (PanaX. Etec Co.).

Characterization techniques

Morphologies of HI-CNT/Fe_2O_3 nanofibers were examined by field-emission scanning electron microscopy (FE-SEM, ULTRA PLUS, ZEISS) and field-emission transmission electron microscopy (FE-TEM, JEOL, JEM-2100F). Phases were analyzed by X-ray diffractometry (XRD, D8 Discover with GADDS, Bruker) using Cu K_α radiation (λ = 1.5418 Å). Structures of carbonaceous materials in the composite were characterized at room temperature *via* Raman spectroscopy (Jobin Yvon LabRam, HR800, excitation source = 514 nm He–Ne laser). X-ray photoelectron spectroscopy (XPS, Thermo Scientific K-Alpha) with focused monochromatic Al K_α radiation at 12 kV and 20 mA was used to analyze the composition of these nanofibers. The surface area of the sample was measured using the Brunauer–Emmett–Teller (BET) method with N_2 as the adsorbate gas. Thermogravimetric (TG) analysis was performed using a Pyris 1 TGA (Perkin Elmer) within the temperature range of 25–700 °C at a heating rate of 10 °C min^{-1} in air.

Electrochemical measurements

Electrochemical properties of self-supported HI-CNT/Fe_2O_3 nanofibers were analyzed by constructing pouch-type flexible-cells using the PI-based gel-polymer electrolyte without a separator. For a half-cell, lithium metal was used as the counter electrode. The gel-polymer electrolyte was prepared by soaking the PI matrix in a solution of 1 M $LiPF_6$ in ethylene carbonate (EC)/dimethyl carbonate (DMC) (1 : 1 by vol.). The anode was prepared by mixing HI-CNT/Fe_2O_3 nanofibers, carbon black, and poly vinylidene fluoride (PVDF) in a weight ratio of 8 : 1 : 1. Charge/discharge characteristics of samples were measured at various current densities in the voltage range of 0.001–3.0 V. Cyclic voltammograms (CVs) were recorded at a scan rate of 0.01 mV s^{-1}. The size of the negative electrode containing the sample was 0.95 cm^2 and the mass loading was approximately

2.5 mg cm^{-2}. A pouch-type flexible full-cell was also fabricated using an anode of HI-CNT/Fe_2O_3 nanofibers and a $LiFePO_4$ cathode. Each electrode was prepared by mixing active material, carbon black, and PVDF in a weight ratio of 8 : 1 : 1. The loading mass of the $LiFePO_4$ cathode was 6.1 mg cm^{-2} while that of the anode was kept at 1.9 mg cm^{-2}. Constant current tests were carried out in a voltage window of 2.5–4.0 V. Rate performances were investigated at different current densities ranging from 0.5C (0.23 mA cm^{-2}) to 1C (0.46 mA cm^{-2}). The electrode capacity of the full-cell was calculated according to the weight of the cathode material.

Results and discussion

The synthetic strategy for the highly integrated and interconnected CNT hybrid nanofibers decorated with α-Fe_2O_3 nanoparticles (HI-CNT/Fe_2O_3 nanofibers) as freestanding anodes for flexible lithium polymer batteries is described in Scheme 1. In this study, efficient dispersion of $Fe(acac)_3$, PAN, and acid-treated CNTs in the spinning solution prevented the aggregation of CNTs, a key factor for the formation of these highly integrated and interconnected CNT hybrid nanofibers. In the colloidal spinning solution, aggregation of CNTs induced by van der Waals forces was effectively prevented by the formation of homogeneous complexes of $Fe(acac)_3$–PAN–CNTs in DMF. By modifying CNTs using a HNO_3/H_2SO_4 acid solution, a carboxylic group (–COOH) was attached onto CNTs.[33,34] Subsequently, acid-treated CNTs were added into a DMF solution containing both modified PAN and $Fe(acac)_3$ salt. PAN was also pre-sulfonated. The electrophilic nitrile (–C≡N) group of PAN was hydrolyzed to form a sulfonated polyacrylamide (–SO_3H, O=C–NH_2) group.[35,36] The attachment of carboxylic groups on CNTs and sulfonated polyacrylamide groups on PAN after acid-treatment were directly proven by FT-IR results (Fig. S1†). Carboxylic groups of acid-treated CNTs have dipole–dipole interactions and hydrogen bonding with sulfonated polyacrylamide groups of PAN.[37–39] Additionally, the $Fe(acac)_3$ precursor could be adsorbed onto both acid-treated CNTs and sulfonated polyacrylamide, resulting in the formation of a uniform complex of $Fe(acac)_3$–PAN–CNTs.[40,41] Thus, a stable jet containing highly integrated CNTs was generated without being agglomerated during the electrospinning process. Subsequently, the jet was solidified into nanofibers by DMF evaporation from the nanofiber surface. As a result, $Fe(acac)_3$/PAN/CNT composite precursor nanofibers were obtained following the spinning process. Subsequently, α-Fe_2O_3 nanoparticles were formed around CNTs by the conversion of the precursor $Fe(acac)_3$ during a simple heat-treatment process at 350 °C. Concurrently, modified PAN in the composite was selectively removed by carbonization and subsequent decomposition into CO_2 gas, leading to the formation of numerous mesopores around CNTs. Through a series of procedures, highly integrated and interconnected CNT hybrid nanofibers decorated with α-Fe_2O_3 nanoparticles were finally obtained, as described in Scheme 1.

The synthetic strategy for HI-CNT/Fe_2O_3 nanofibers was determined by examining morphological and phase changes of nanofiber structures induced by each step. Nanofiber morphologies, the FT-IR spectrum, and the XRD pattern of the as-spun $Fe(acac)_3$/PAN/CNT composite nanofibers are shown in Fig. 1. After spinning, the composite nanofibers exhibited a uniform diameter of 500 nm and a rough nanofiber surface as shown in Fig. 1a and b. CNTs were highly integrated and

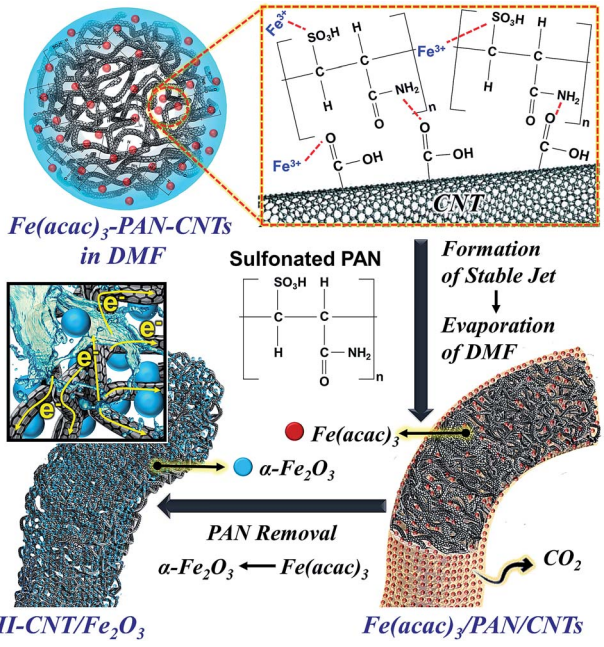

Scheme 1 Detailed formation mechanism of HI-CNT/Fe_2O_3 nanofibers by electrospinning and subsequent heat-treatment.

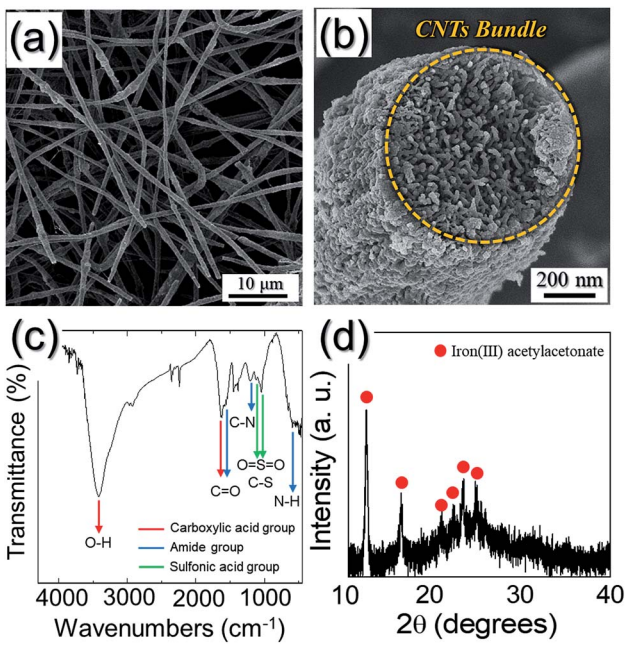

Fig. 1 (a and b) FE-SEM images, (c) FT-IR spectrum, and (d) XRD pattern of the as-spun $Fe(acac)_3$/PAN/CNT composite nanofibers obtained after electrospinning.

interconnected as a bundle in the as-spun nanofiber structure as indicated by the cross-sectional FE-SEM image shown in Fig. 1b. Acid-treated CNTs with a carboxylic group (–COOH) have dipole–dipole interactions and hydrogen bonding with sulfonated polyacrylamide groups (–SO_3H, O=C–NH_2) of modified PAN. Related functional groups were verified in FT-IR results shown in Fig. 1c. The functional group of sulfonated-polyacrylamide for sulfonated PAN was determined by the amide group (NH_2–C=O) and sulfonic acid group (SO_3H) characterized by five peaks of N–H, C–N, C=O, O=S=O, and C–S. Therefore, 588 cm^{-1} (N–H), 1214 cm^{-1} (C–N), 1580 cm^{-1} (C=O), 1197 cm^{-1} (O=S=O), and 1040 cm^{-1} (C–S) were definitely confirmed in Fig. 1c.[36,42] Peaks located at 1640 cm^{-1} (C=O) and 3400 cm^{-1} (O–H) corresponding to the carboxylic acid group (–COOH) attached onto surfaces of the acid-treated CNTs were also confirmed.[34,43] The as-spun nanofibers were composed of the precursor $Fe(acac)_3$, modified PAN, and acid-treated CNTs, in which the phase of $Fe(acac)_3$ was confirmed in the XRD pattern as shown in Fig. 1d.[44] The TG curve of the as-spun nanofibers shown in Fig. S2† exhibited a three-step weight loss up to 600 °C. The first weight loss of 10% up to 250 °C was caused by evaporation of adsorbed water in the structure. The second weight loss of 62% between 250 °C and 300 °C was attributed to decomposition of modified PAN in composite nanofibers. CNTs constituting the nanofibers were decomposed at temperatures above 500 °C. Therefore, appropriate heat-treatment temperature of the resulting nanofibers should be below 500 °C to maintain the CNT framework.

HI-CNT/Fe_2O_3 nanofibers were obtained after heat-treating the as-spun $Fe(acac)_3$/PAN/CNT composite nanofibers at 350 °C in an air atmosphere. A heat-treatment temperature of 350 °C was suitable for selectively removing modified PAN in the as-spun $Fe(acac)_3$/PAN/CNT composite. At this temperature, CNTs were not decomposed as confirmed by TGA results of the as-spun $Fe(acac)_3$/PAN/CNT composite nanofibers shown in Fig. S2a.† The resulting HI-CNT/Fe_2O_3 nanofibers showed much rougher nanofiber surfaces than the as-spun nanofibers as shown in Fig. 2a. During heat-treatment, the PAN content in the composite was decomposed into gaseous CO_2 and then removed, leading to CNT exposure on the nanofiber surface. These highly integrated CNTs (as indicated by arrows) and the CNT bundle constituting these nanofibers are shown in the fractured FE-SEM image (Fig. 2b). These CNTs were connected to provide a conductive path for electrons for a fast discharge/charge process during repeated cycles. Highly integrated and interconnected CNTs in the structure were further verified by TEM images shown in Fig. 2c and d. In particular, numerous mesopores formed by PAN decomposition in the composite around CNTs during heat-treatment were observed in Fig. 2c. Mesopores in the composite could provide additional contact surfaces between active materials and the electrolyte which could promote fast ionic/electronic diffusion, resulting in improved rate properties of the electrode. Numerous interconnected CNTs with lattice fringes separated by 0.34 nm corresponding to the (002) plane of CNTs were observed in the high-resolution TEM (HR-TEM) image shown in Fig. 2d. Additionally, α-Fe_2O_3 nanocrystals (as indicated by stars)

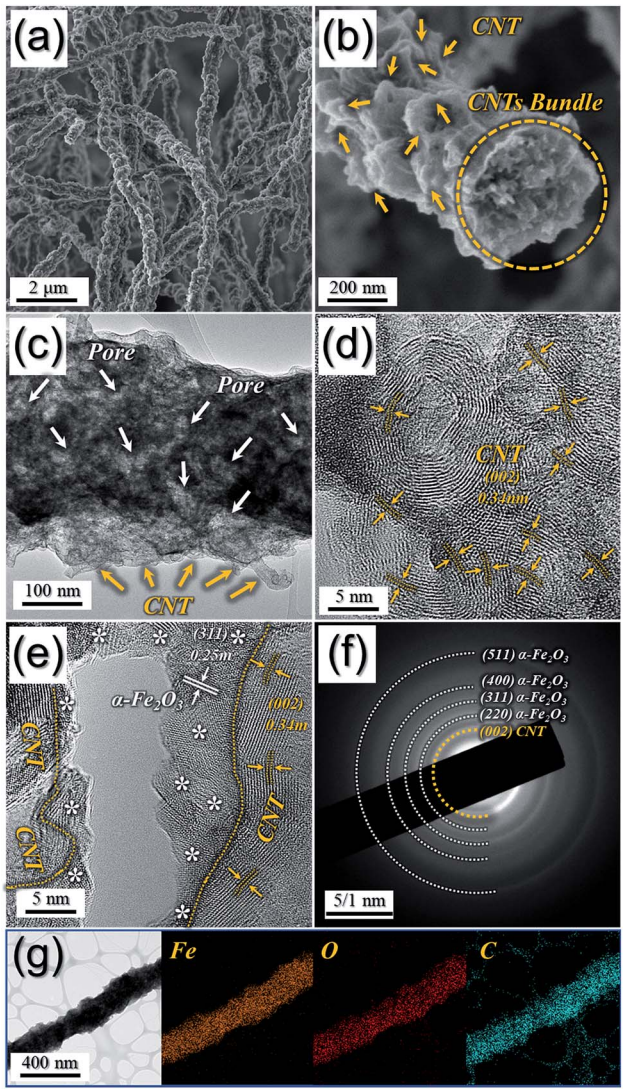

Fig. 2 Morphologies, SAED pattern, and elemental mapping images of HI-CNT/Fe_2O_3 nanofibers obtained after heat-treatment at 350 °C: (a and b) FE-SEM images, (c) TEM image, (d and e) HR-TEM images, (f) SAED pattern, and (g) elemental mapping images.

formed by conversion from the precursor $Fe(acac)_3$ during heat-treatment were decorated around CNTs as shown in Fig. 2e. As shown in Fig. 2e, lattice fringes displaying an interplanar spacing of 0.25 nm matching well with the (311) plane of α-Fe_2O_3 were confirmed.[45,46] The growth of α-Fe_2O_3 nanocrystals in the composite was effectively interrupted when surrounded by carbon decomposed from PAN and CNTs during heat-treatment at a low temperature of 350 °C, leading to small crystallite sized α-Fe_2O_3 nanoparticles of around 5 nm. Nano-sized α-Fe_2O_3 could ensure short transport length for Li^+ ions and electrons during the charge/discharge process, resulting in enhanced rate capability. Additionally, it decreases stress induced by the severe volume variation of α-Fe_2O_3 upon cycling, leading to improved capacity retention. The selected area diffraction (SAED) pattern shown in Fig. 2f further proved the formation of α-Fe_2O_3 nanocrystals around

the CNT framework. Elemental mapping images shown in Fig. 2g confirmed the homogeneous distribution of Fe, O, and C elements, implying that ultrafine α-Fe_2O_3 nanocrystals were uniformly adorned on the highly integrated CNT framework.

Characteristics of the resulting HI-CNT/Fe_2O_3 nanofibers are shown in Fig. 3. Both low-crystalline α-Fe_2O_3 and CNT phases were confirmed from XRD results of HI-CNT/Fe_2O_3 nanofibers shown in Fig. 3a. The presence of α-Fe_2O_3 was later confirmed more clearly by Raman spectroscopy. Chemical information of HI-CNT/Fe_2O_3 nanofibers was investigated by analyzing the XPS spectra shown in Fig. 3b–d. The spectrum was deconvoluted by Gaussian curve fitting to estimate the proportions of phases. In Fig. 3b, the survey XPS spectrum revealed the presence of the elements Fe, C, and O in the structure. The high-resolution Fe 2p XPS spectrum (Fig. 3c) clearly showed both Fe^{3+} peaks at 710.3 and 723.8 eV and Fe^{2+} peaks at 712.2 and 725.6 eV along with their satellite peaks at 719.3 and 733.2 eV, in good agreement with results previously reported in the literature for α-Fe_2O_3.[47,48] In the C 1s XPS spectrum shown in Fig. 3d, intense peaks located at 246.3, 285.7, and 286.5 eV corresponded to C–C/C=C, C–O, and C=O, respectively.[49,50] The C–O and C=O peaks originated from general heat-treated CNTs with oxygen-containing groups formed during treatment at 350 °C. Raman spectroscopy was also employed to investigate the electronic structure and degree of graphitization of HI-CNT/Fe_2O_3 nanofibers as shown in Fig. 3e and f. Five strong resonance peaks at 221, 287, 405, 497, and 609 cm^{-1} in the range of 100–700 cm^{-1} were observed as shown in Fig. 3e, consistent with typical frequencies observed for α-Fe_2O_3.[51,52] In addition, D-(1345 cm^{-1}) and G-bands (1593 cm^{-1}) generally used as measures of structural disorder in graphitic materials were detected in Fig. 3f.[53] The relative intensity ratio of D to G bands (I_D/I_G) of HI-CNT/Fe_2O_3 nanofibers was approximately 1.28. The disorder of CNTs might be attributed to the presence of substitutional heteroatom vacancies and other defects on nanotube-walls formed by both acid-treatment of CNTs using the HNO_3/H_2SO_4 solution and heat-treatment at 350 °C.[54,55] In the same context, the D′ band at 1620 cm^{-1} suggesting high defect densities in the CNTs was also confirmed in Fig. 3f.[56] The Brunauer–Emmett–Teller (BET) surface area of HI-CNT/Fe_2O_3 nanofibers was 160 $m^2\ g^{-1}$, which is much higher than that of the as-spun $Fe(acac)_3$/PAN/CNT nanofibers (20 $m^2\ g^{-1}$) as shown in Fig. S3.† This high BET value was due to the following factors: (1) the existence of CNTs, (2) mesopores formed by PAN decomposition around CNTs, and (3) defects formed by both acid- and heat-treatment of CNTs. The Barrett–Joyner–Halenda (BJH) and density functional theory (DFT) pore size distributions of HI-CNT/Fe_2O_3 nanofibers in Fig. S3 and S4† showed micropores with diameters under 2 nm due to CNTs and mesopores around 20 nm attributed to pores between CNTs and pores formed by PAN decomposition. The CNT content in the structure of HI-CNT/Fe_2O_3 nanofibers was estimated by TGA as shown in Fig. S2b.† The 10% weight loss up to 200 °C is attributed to evaporation of adsorbed water. Additionally, a small amount of residual C decomposed from PAN in the as-spun nanofibers during heat-treatment at 350 °C was decomposed into CO_2 gas, resulting in a weight loss of 5% between 350 and 450 °C. The 38% weight loss over 450 °C proved that a large amount of CNTs (38 wt%) were included in HI-CNT/Fe_2O_3 nanofibers. In order to apply the resulting HI-CNT/Fe_2O_3 nanofibers as self-supported anodes for flexible lithium polymer batteries, HI-CNT/Fe_2O_3 nanofibers were finally prepared in the form of a sheet as shown in Fig. 4a. The self-supported working electrode showed excellent flexibility and robustness as it could be bent back and forth. The sheet of HI-CNT/Fe_2O_3 nanofibers was composed of thorny-bush-shaped nanofibers interconnected with each other. The free-standing PI matrix as a gel polymer electrolyte (GPE) was also fabricated by electrospinning for the flexible battery as shown in Fig. 4b. PAA nanofibers were transformed into PI nanofibers with high thermal and mechanical stability by imidization. Fig. 4b shows the FE-SEM image of the freestanding PI matrix that consists of a well-connected porous structure with a diameter of 400–800 nm, similar to the overall morphology. The interconnected nanofiber network of the PI matrix provided good impregnation of the electrolyte to obtain high ionic conductivity. The yellow colored PI matrix had a high thermal stability of 550 °C and a high mechanical strength of 37 MPa.[32]

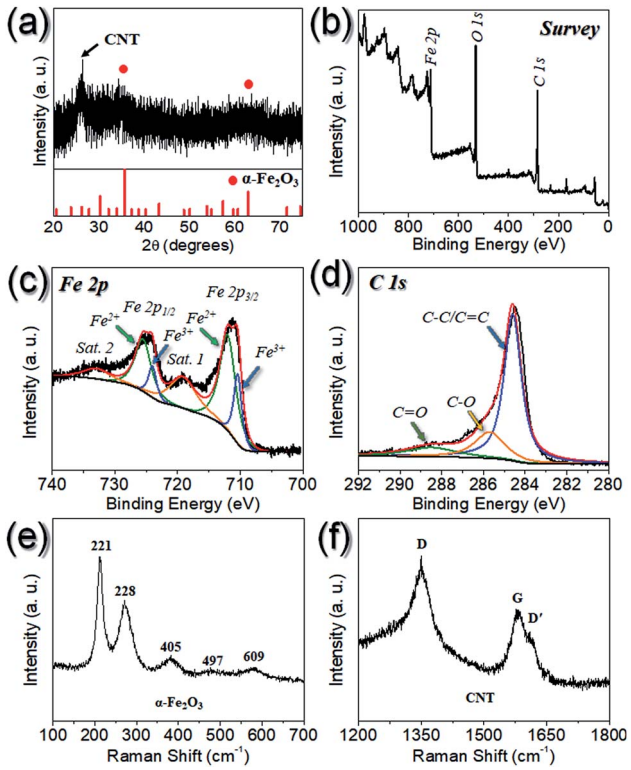

Fig. 3 Characteristics of HI-CNT/Fe_2O_3 nanofibers obtained after heat-treatment at 350 °C: (a) XRD pattern, (b) XPS survey spectrum, (c) Fe 2p XPS spectrum, (d) C 1s XPS spectrum, and Raman spectra in the range of (e) 100–700 cm^{-1}, and (f) 1200–1800 cm^{-1}.

CV curves of HI-CNT/Fe_2O_3 nanofibers for the first five cycles at a scan rate of 0.1 mV s^{-1} in the 0.001–3.0 V range are shown in Fig. 5a. A distinct reduction peak at around 0.7 V was observed in the first cathodic sweep. This was attributed to the

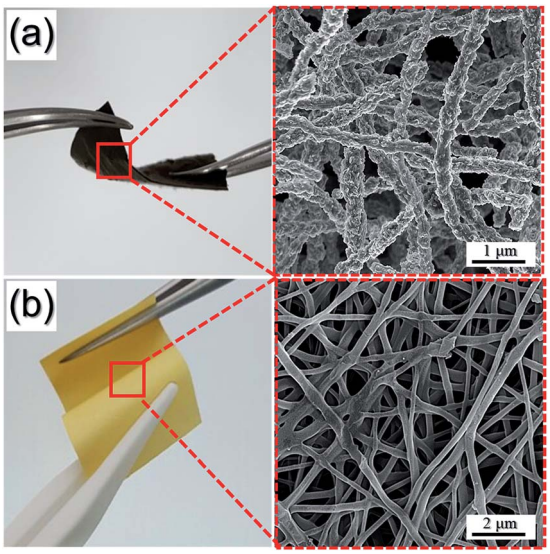

Fig. 4 Photographs of (a) a HI-CNT/Fe_2O_3 nanofiber sheet as a self-supported anode and (b) the PI matrix as a gel polymer electrolyte.

reduction of α-Fe_2O_3 to metallic Fe and the formation of amorphous Li_2O as well as the decomposition of organic electrolyte to form a solid electrolyte interphase (SEI) layer.[45,46,57] The peak at 0.05 V was associated with Li^+ ion intercalation into CNTs in the composite.[58,59] Additionally, the reductive peak at around 1.5 V was due to the reaction between functional groups of CNTs and lithium metal.[59,60] In order to prove this, pure CNTs were acid-treated and subsequently heat-treated at 350 °C and the CV curve of the treated CNTs was shown in Fig. S5.† A broad peak at around 1.5 V was observed, which is attributed to the reaction between functional groups of CNTs and lithium metal. The peak became very weak upon subsequent cycles, indicating that an irreversible reaction happened only during the first cycle. During the charging process, oxidation of Fe to Fe_3O_4 and Fe_3O_4 to Fe_2O_3 occurred at around 1.6 and 1.8 V, respectively.[45,46,57] The anodic peak at 0.25 V was attributed to de-intercalation of Li^+ ions from CNTs. Another peak at around 1.0 V was attributed to partial decomposition of the SEI layer.[58,59] The main reduction peak at around 0.7 V shifted to a slightly higher potential after the first cycle due to the formation of ultrafine nanocrystals during the first cycle. The good overlapping of the CV curves from the third cycle onward revealed good reversibility of electrochemical reactions.[45,46] Discharge–charge curves of HI-CNT/Fe_2O_3 nanofibers as free-standing anodes for the first, third, and fifth cycles at 0.1C are shown in Fig. 5b. During the discharge process in the first cycle, two flat sections were observed (at 1.5 V due to the reaction between CNTs and lithium metal, and at 0.7 V due to the reduction of α-Fe_2O_3 to metallic Fe and the formation of amorphous Li_2O). Charge profiles showed a plateau from 1.0 to 1.8 V, corresponding to the oxidation of Fe nanocrystals. The first discharge capacity was 1007 mA h g^{-1} and the subsequent charge capacity was 791 mA h g^{-1}, resulting in an irreversible capacity loss of 20%. This irreversible capacity loss was due to electrolyte decomposition and formation of the SEI on the surface of HI-CNT/Fe_2O_3 nanofibers. In the second cycle, the capacity decreased to 792 mA h g^{-1}. It then remained stable in the following cycles. Considering the theoretical specific capacity of Fe_2O_3 (1007 mA h g^{-1}) and C (372 mA h g^{-1}), the theoretical capacity of HI-CNT/Fe_2O_3 nanofibers is about 766 mA h g^{-1}. The extra capacity of HI-CNT/Fe_2O_3 nanofibers may be due to the partially reversible formation and decomposition of the gel-like SEI film on the surface of the electrode and pseudo capacitance.[61] The high capacity of HI-CNT/Fe_2O_3 nanofibers was attributed to the unique structure combining the following advantages: high capacity contributed by α-Fe_2O_3, fast ionic/electronic transport within the interconnected CNT framework, and large contact area of α-Fe_2O_3 with the electrolyte. These provided fast lithium ion transport into the flexible electrode.

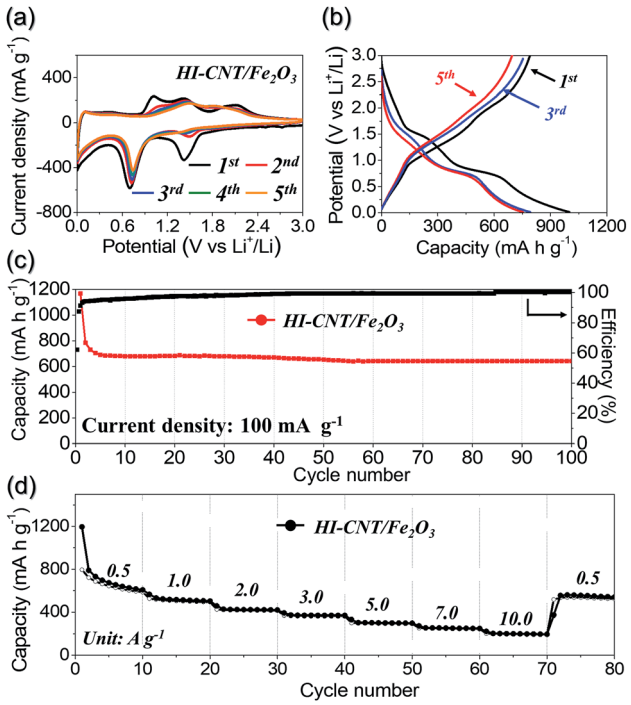

Fig. 5 Electrochemical properties of the free-standing HI-CNT/Fe_2O_3 nanofiber electrode using the PI electrolyte: (a) CV curve, (b) charge–discharge profile, (c) cycling performance at a current density of 100 mA g^{-1}, and (d) rate performance.

The cycling performance of the freestanding HI-CNT/Fe_2O_3 nanofiber cell was further evaluated. As shown in Fig. 5c, even after 100 cycles, the discharge capacity of HI-CNT/Fe_2O_3 nanofibers remained at 651 mA h g^{-1}. Its capacity retention measured from the fifth cycle was 94%. Although the Coulombic efficiency during the first cycle was 80%, it quickly increased to 91.7% during the third cycle and then further increased to 99% during the 100th cycle. Mesopores in the composite and constituent CNT framework allow for a degree of buffering against volume changes of α-Fe_2O_3 particles associated with phase transitions occurring during repeated cycles, staving off the pulverization and agglomeration of the electrode, thereby improving the cycling life of freestanding anodes. In order to calculate the capacity contribution of the CNT

framework to the HI-CNT/Fe_2O_3 nanofiber electrode, HI-CNT/Fe_2O_3 nanofibers were etched with HCl solution, thus obtaining pure CNT fibers as shown in Fig. S6.† Complete removal of α-Fe_2O_3 from the structure was proven by EDS as shown in Fig. S6b.† The first discharge–charge profile confirmed that the CNT framework was pure carbon with discharge and charge capacities of 828 and 343 mA h g^{-1}, respectively, as shown in Fig. S6c.† The pure CNT framework exhibited a reversible discharge capacity of 248 mA h g^{-1} at a current density of 100 mA g^{-1} for the 100th cycle as shown in Fig. S6d.† Therefore, the contribution of the CNT framework to the discharge capacity of the HI-CNT/Fe_2O_3 nanofiber electrode could be estimated to be 13.7%. The rate performance of freestanding HI-CNT/Fe_2O_3 nanofibers is shown in Fig. 5d in which the current density is increased step-wise from 0.5 to 10.0 A g^{-1}. These highly integrated and interconnected CNTs in the composite resulted in good rate performance. HI-CNT/Fe_2O_3 nanofibers had final discharge capacities of 608, 503, 420, 369, and 299 mA h g^{-1} at current densities of 0.5, 1.0, 2.0, 3.0, 5.0, 7.0, and 10.0 A g^{-1}, respectively. When the current density decreased to 0.5 A g^{-1}, the capacity of HI-CNT/Fe_2O_3 nanofibers nearly recovered to 540 mA h g^{-1}, even after cycling at high current densities. These results indicate that the Li^+ ion storage performance of HI-CNT/Fe_2O_3 nanofibers is not degraded, even at high current densities. The morphology of HI-CNT/Fe_2O_3 nanofibers obtained after 100 cycles for anodes are shown in Fig. 6. HI-CNT/Fe_2O_3 nanofibers maintained their original morphologies well even after repeated lithium insertion and desertion processes. Their unique structure could effectively accommodate severe volume variations of α-Fe_2O_3, thus enhancing the structural stability of HI-CNT/Fe_2O_3 nanofibers and leading to improved Li^+ ion storage properties. Moreover, the interfacial resistance as shown in Fig. S7† is much increased after the first cycle due to the formation of the SEI layer but it is decreased and stabilized with cycling due to the unique structure.

In order to prepare a freestanding flexible full Li^+ ion cell, an anode of HI-CNT/Fe_2O_3 nanofibers was combined with a $LiFePO_4$ fiber cathode. The discharge–charge profile of the flexible $LiFePO_4$ cathode in a half-cell is shown in Fig. S8† along with its cycle performance at a current density of 0.2 A g^{-1}. Charge–discharge profiles of the freestanding flexible HI-CNT/Fe_2O_3 nanofiber@GPE@$LiFePO_4$ full-cell at 0.5C are shown in Fig. 7a.

The process provided a first discharge capacity of 152.5 mA h g^{-1} and a subsequent charge capacity of 155.4 mA h g^{-1}, resulting in an irreversible capacity loss of 2%. The discharge capacity reached 89% of the theoretical capacity of the $LiFePO_4$ cathode. In addition, in the second and fifth cycles, both discharge capacities were 151 mA h g^{-1}. Their corresponding charge capacities were 150.4 mA h g^{-1} and 150.0 mA h g^{-1}, respectively. Moreover, Coulombic efficiencies in the second and fifth cycles were 99%. The increased Coulombic efficiency with cycling is due to interfacial instabilities and improved penetration of ions. The high capacity and Coulombic efficiency are due to the outstanding ability of the flexible HI-CNT/Fe_2O_3 nanofiber electrode and the PI-based gel polymer electrolyte to rapidly transfer electrons and ions. Optical images of the freestanding flexible full-cell battery connected to a red light-emitting diode (LED) are shown in Fig. 7b. The battery continuously powered the LED after flexing ten times to a bend with 90°. The brightness of the LED remained constant during this period. Fig. 7c shows the cycle properties of the flexible HI-CNT/Fe_2O_3 nanofiber@GPE@$LiFePO_4$ full-cell in bent (90°) and flat states. The specific capacity was maintained at 146 mA h g^{-1} even after 10 cycles of bending as compared with 144 mA h g^{-1} before bending (*i.e.*, only a slight decrease of 1.3%). In addition, their capacities well recovered to 148.5 mA h g^{-1} when the full-cell was re-flattened. In commercial lithium ion cells, bending can lead to delamination or cracking–swelling of the electrode or membrane, inducing a rapid capacity drop. However, the capacity of the flexible HI-CNT/Fe_2O_3 nanofiber@GPE@$LiFePO_4$ battery did not drop significantly even after 90° bending.

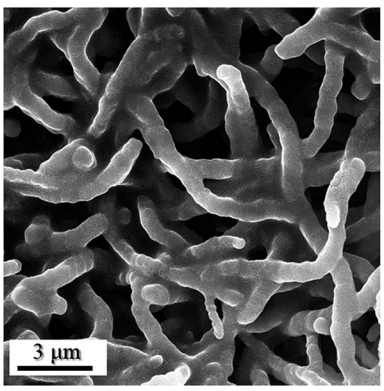

Fig. 6 FE-SEM image of the free-standing HI-CNT/Fe_2O_3 nanofiber electrode after 100 cycles.

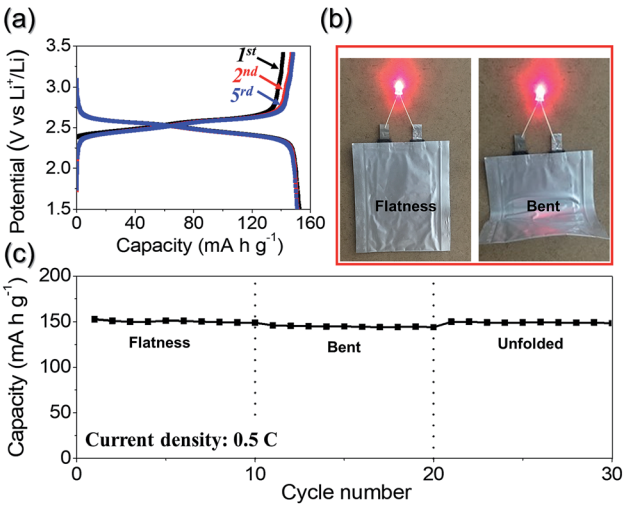

Fig. 7 Electrochemical properties of the freestanding flexible HI-CNT/Fe_2O_3 nanofiber@GPE@$LiFePO_4$ full-cell: (a) charge/discharge profile, (b) digital photographic image of a light-emitting diode, and (c) cycling performance in bent (90°) and flat states at a current density of 0.5C.

Conclusions

In this study, highly integrated and interconnected CNT hybrid nanofibers decorated with α-Fe_2O_3 nanoparticles were prepared for the first time by electrospinning with subsequent heat-treatment as freestanding anodes for flexible lithium polymer batteries. The efficient dispersion of $Fe(acac)_3$, PAN, and acid-treated CNTs in the spinning solution prevented the aggregation of CNTs, a key factor for the formation of HI-CNT/Fe_2O_3 nanofibers. Carboxylic groups of acid-treated CNTs have dipole–dipole interactions and hydrogen bonding with sulfonated polyacrylamide groups of PAN. In addition, the $Fe(acac)_3$ precursor could be adsorbed onto both acid-treated CNTs and sulfonated polyacrylamide, resulting in the formation of a complex of $Fe(acac)_3$–PAN–CNTs. The complete conversion of the precursor $Fe(acac)_3$ into α-Fe_2O_3 and the decomposition of PAN in the composite during heat-treatment resulted in the formation of HI-CNT/Fe_2O_3 nanofibers which showed excellent Li^+ ion storage properties as freestanding flexible anodes. The synthetic strategy introduced in this study can be applied to the preparation of highly integrated and interconnected CNT hybrid nanofibers decorated with various transition-metal compounds for a wide variety of applications, including energy storage.

Conflicts of interest

There are no conflicts to declare.

Acknowledgements

This work was supported by grants (NRF-2018R1A4A1024691, NRF-2017M1A2A2087577, and NRF-2018R1D1A3B07042514) from the National Research Foundation of Korea (NRF) funded by the Korean government (MSIP).

References

1 M. Li, J. Meng, Q. Li, M. Huang, X. Liu, K. A. Owusu, Z. Liu and L. Mai, *Adv. Funct. Mater.*, 2018, **28**, 1802016.
2 L. Noerochim, J.-Z. Wang, S.-L. Chou, D. Wexler and H.-K. Liu, *Carbon*, 2012, **50**, 1289–1297.
3 H. Yu, C. Zhu, K. Zhang, Y. Chen, C. Li, P. Gao, P. Yang and Q. Ouyang, *J. Mater. Chem. A*, 2014, **2**, 4551–4557.
4 Z. Zhang, T. Zhai, X. Lu, M. Yu, Y. Tong and K. Mai, *J. Mater. Chem. A*, 2013, **1**, 505–509.
5 J.-E. Lim and J.-K. Kim, *Korean J. Chem. Eng.*, 2018, **35**, 2464–2467.
6 M. H. Tahmasebi, D. Kramer, R. Mönig and S. T. Boles, *J. Electrochem. Soc.*, 2019, **166**, A5001–A5007.
7 J. Wang, C. Wang and M. Zhen, *Chem. Eng. J.*, 2019, **356**, 1–10.
8 L. Xia, S. Wang, G. Liu, L. Ding, D. Li, H. Wang and S. Qiao, *Small*, 2016, **12**, 853–859.
9 Y. Yan, C. Li, C. Liu, Z. Mutlu, B. Dong, J. Liu, C. S. Ozkan and M. Ozkan, *Carbon*, 2019, **142**, 238–244.
10 A. M. Chockla, J. T. Harris, V. A. Akhavan, T. D. Bogart, V. C. Holmberg, C. Steinhagen, C. B. Mullins, K. J. Stevenson and B. A. Korgel, *J. Am. Chem. Soc.*, 2011, **133**, 20914–20921.
11 J. Lee and J. H. Moon, *Korean J. Chem. Eng.*, 2017, **34**, 3195–3199.
12 Y. Liu, A. A. Elzatahry, W. Luo, K. Lan, P. Zhang, J. Fan, Y. Wei, C. Wang, Y. Deng and G. Zheng, *Nano Energy*, 2016, **25**, 80–90.
13 Z. Yan, Q. Hu, G. Yan, H. Li, K. Shih, Z. Yang, X. Li, Z. Wang and J. Wang, *Chem. Eng. J.*, 2017, **321**, 495–501.
14 X. Yang, Y. Yang, H. Hou, Y. Zhang, L. Fang, J. Chen and X. Ji, *J. Phys. Chem. C*, 2015, **119**, 3923–3930.
15 S. Li, H. Tang, P. Ge, F. Jiang, J. Zhou, C. Zhang, H. Hou, W. Sun and X. Ji, *ACS Appl. Mater. Interfaces*, 2018, **10**, 6378–6389.
16 H. Liu, S. Chen, G. Wang and S. Qiao, *Chem.–Eur. J.*, 2013, **19**, 16897–16901.
17 S. H. Oh, J.-S. Park, M. S. Jo, Y. C. Kang and J. S. Cho, *Chem. Eng. J.*, 2018, **347**, 889–899.
18 H. Park, D. H. Yeom, J. Kim and J. K. Lee, *Korean J. Chem. Eng.*, 2015, **32**, 178–183.
19 J. Wang, Q. Zhang, X. Li, D. Xu, Z. Wang, H. Guo and K. Zhang, *Nano Energy*, 2014, **6**, 19–26.
20 M.-S. Balogun, Z. Wu, Y. Luo, W. Qiu, X. Fan, B. Long, M. Huang, P. Liu and Y. Tong, *J. Power Sources*, 2016, **308**, 7–17.
21 J. S. Cho, Y. J. Hong and Y. C. Kang, *ACS Nano*, 2015, **9**, 4026–4035.
22 M. V. Reddy, T. Yu, C.-H. Sow, Z. X. Shen, C. T. Lim, G. V. S. Rao and B. V. R. Chowdari, *Adv. Funct. Mater.*, 2007, **17**, 2792–2799.
23 J. S. Cho, J. S. Park and Y. C. Kang, *Sci. Rep.*, 2016, **6**, 38933.
24 J. Chen, L. Xu, W. Li and X. Gou, *Adv. Mater.*, 2005, **17**, 582–586.
25 J. S. Cho, J.-S. Park, K. M. Jeon and Y. C. Kang, *J. Mater. Chem. A*, 2017, **5**, 10632–10639.
26 J. H. Kim, Y. J. Hong, Y. C. Kang, Y. J. Choi and Y. S. Kim, *Electrochim. Acta*, 2015, **154**, 211–218.
27 G. Gao, Q. Zhang, X.-B. Cheng, P. Qiu, R. Sun, T. Yin and D. Cui, *ACS Appl. Mater. Interfaces*, 2015, **7**, 340–350.
28 W. J. Yu, P. X. Hou, L. L. Zhang, F. Li, C. Liu and H. M. Cheng, *Chem. Commun.*, 2010, **46**, 8576–8578.
29 B. M. Bak, S.-K. Kim and H. S. Park, *Mater. Chem. Phys.*, 2014, **144**, 396–401.
30 Y. Zhao, J. Li, Y. Ding and L. Guan, *Chem. Commun.*, 2011, **47**, 7416–7418.
31 N. Yan, X. Zhou, Y. Li, F. Wang, H. Zhong, H. Wang and Q. Chen, *Sci. Rep.*, 2013, **3**, 3392.
32 J.-E. Lim, M.-S. Oh, J.-H. Ahn and J.-K. Kim, *Electrochim. Acta*, 2017, **238**, 107–111.
33 F. H. Gojny, J. Nastalczyk, Z. Roslaniec and K. Schulte, *Chem. Phys. Lett.*, 2003, **370**, 820–824.
34 I. D. Rosca, F. Watari, M. Uo and T. Akasaka, *Carbon*, 2005, **43**, 3124–3131.
35 T. Do, H. Lee, Y. G. Ko, Y. Chun, U. S. Choi and C. H. Kim, *Colloids Surf., A*, 2017, **514**, 56–62.

36 A. Touheed and H. Maab, *J. Chin. Chem. Soc.*, 2012, **59**, 1541–1547.
37 E. V. Basiuk, V. A. Basiuk, J.-G. Bañuelos, J.-M. Saniger-Blesa, V. A. Pokrovskiy, T. Y. Gromovoy, A. V. Mischanchuk and B. G. Mischanchuk, *J. Phys. Chem. B*, 2002, **106**, 1588–1597.
38 H. J. Kim, K. Choi, Y. Baek, D.-G. Kim, J. Shim, J. Yoon and J.-C. Lee, *ACS Appl. Mater. Interfaces*, 2014, **6**, 2819–2829.
39 S. Mallakpour and A. Zadehnazari, *Carbon*, 2013, **56**, 27–37.
40 J. Du and X. Zhang, *J. Appl. Polym. Sci.*, 2008, **109**, 2935–2941.
41 J. Hu, M. Chen, X. Fang and L. Wu, *Chem. Soc. Rev.*, 2011, **40**, 5472–5491.
42 Y. Feng, H. Liu, W. Luo, E. Liu, N. Zhao, K. Yoshino and W. Feng, *Sci. Rep.*, 2013, **3**, 3260.
43 E. M. Jin, H. J. Lee, H.-B. Jun and S. M. Jeong, *Korean J. Chem. Eng.*, 2017, **34**, 885–891.
44 A. Dakhel and A. A. Mohamed, *J. Phys. Chem. Solids*, 2007, **68**, 162–167.
45 S.-K. Park, J. H. Choi and Y. C. Kang, *J. Mater. Chem. A*, 2018, **6**, 8462–8469.
46 J. S. Cho, Y. J. Hong and Y. C. Kang, *Nanoscale*, 2015, **18**, 8361–8367.
47 J. Feng, D. Fan, Q. Wang, L. Ma, W. Wei, J. Xie and J. Zhu, *Colloids Surf., A*, 2017, **520**, 743–756.
48 G. Li, X. Xu, R. Han and J. Ma, *CrystEngComm*, 2016, **18**, 2949–2955.
49 J. H. Kim, Y. J. Oh and Y. C. Kang, *Carbon*, 2018, **128**, 125–133.
50 G. D. Park, J.-K. Lee and Y. C. Kang, *Carbon*, 2018, **128**, 191–200.
51 S. Li, H. Zhang, J. Wu, X. Ma and D. Yang, *Cryst. Growth Des.*, 2006, **6**, 351–353.
52 L. Wang, X. Lu, C. Han, R. Lu, S. Yang and X. Song, *CrystEngComm*, 2014, **16**, 10618–10623.
53 Y. J. Hong, J. S. Cho and Y. C. Kang, *Chem.–Eur. J.*, 2015, **21**, 18202–18208.
54 V. Datsyuk, M. Kalyva, K. Papagelis, J. Parthenios, D. Tasis, A. Siokou, I. Kallitsis and C. Galiotis, *Carbon*, 2008, **46**, 833–840.
55 H. Murphy, P. Papakonstantinou and T. T. Okpalugo, *J. Vac. Sci. Technol., B: Microelectron. Nanometer Struct.–Process., Meas., Phenom.*, 2006, **24**, 715–720.
56 W. Bai, A. Raghavendra, R. Podila and J. M. Brown, *Int. J. Nanomed.*, 2016, **11**, 4357.
57 H. Liu, G. Wang, J. Park, J. Wang, H. Liu and C. Zhang, *Electrochim. Acta*, 2009, **54**, 1733–1736.
58 H. Y. Jung, S. Hong, A. Yu, S. M. Jung, S. K. Jeoung and Y. J. Jung, *RSC Adv.*, 2015, **5**, 68875–68880.
59 S.-K. Park, G. D. Park and Y. C. Kang, *Nanoscale*, 2018, **10**, 11150–11157.
60 S. Klink, E. Ventosa, W. Xia, F. La Mantia, M. Muhler and W. Schuhmann, *Electrochem. Commun.*, 2012, **15**, 10–13.
61 L. Su, Y. Zhong and Z. Zhou, *J. Mater. Chem. A*, 2013, **1**, 15158–15166.